

Journal of Biomedical Optics

BiomedicalOptics.SPIEDigitalLibrary.org

***In vivo* high-resolution cortical imaging with extended-focus optical coherence microscopy in the visible- NIR wavelength range**

Paul J. Marchand
Daniel Szlag
Arno Bouwens
Theo Lasser

SPIE.

Paul J. Marchand, Daniel Szlag, Arno Bouwens, Theo Lasser, “*In vivo* high-resolution cortical imaging with extended-focus optical coherence microscopy in the visible-NIR wavelength range,” *J. Biomed. Opt.* **23**(3), 036012 (2018), doi: 10.1117/1.JBO.23.3.036012.

In vivo high-resolution cortical imaging with extended-focus optical coherence microscopy in the visible-NIR wavelength range

Paul J. Marchand,* Daniel Szlag, Arno Bouwens, and Theo Lasser

Ecole Polytechnique Fédérale de Lausanne, Laboratoire d'Optique Biomédicale, Lausanne, Switzerland

Abstract. Visible light optical coherence tomography has shown great interest in recent years for spectroscopic and high-resolution retinal and cerebral imaging. Here, we present an extended-focus optical coherence microscopy system operating from the visible to the near-infrared wavelength range for high axial and lateral resolution imaging of cortical structures *in vivo*. The system exploits an ultrabroad illumination spectrum centered in the visible wavelength range ($\lambda_c = 650$ nm, $\Delta\lambda \sim 250$ nm) offering a submicron axial resolution (~ 0.85 μm in water) and an extended-focus configuration providing a high lateral resolution of ~ 1.4 μm maintained over ~ 150 μm in depth in water. The system's axial and lateral resolution are first characterized using phantoms, and its imaging performance is then demonstrated by imaging the vasculature, myelinated axons, and neuronal cells in the first layers of the somatosensory cortex of mice *in vivo*. © The Authors. Published by SPIE under a Creative Commons Attribution 3.0 Unported License. Distribution or reproduction of this work in whole or in part requires full attribution of the original publication, including its DOI. [DOI: 10.1117/1.JBO.23.3.036012]

Keywords: optical coherence microscopy; Bessel beams; brain imaging.

Paper 180025R received Jan. 14, 2018; accepted for publication Mar. 7, 2018; published online Mar. 24, 2018.

1 Introduction

Optical coherence tomography (OCT)¹ has emerged in the past decade as a valuable tool to study cerebral physiology,^{2–6} through its ability to perform three-dimensional (3-D) imaging of tissue and vasculature at very high acquisition rates, with A-scan rates typically ranging from 10 to 100 kHz. Although most OCT systems operate in the infrared spectral range to maximize the penetration depth in tissue, recent studies have exploited a visible light source to benefit from the characteristic spectral signatures of certain endo- and exogenous agents at shorter wavelengths.^{7,8} Such spectroscopic OCT systems have been used to increase the contrast of Alzheimeric plaques in brain tissue⁹ and to quantify hemoglobin concentration in the retina^{10,11} and in the brain.^{12,13} Shifting the central wavelength additionally enables increasing the axial resolution of OCT systems as it is determined by $\delta z \propto \lambda_c^2 / \Delta\lambda$, where λ_c is the central wavelength of the source and $\Delta\lambda$ is its bandwidth. Submicron axial resolutions can thus be reached by employing broadband sources in the visible wavelength range.^{9,14–17} A higher lateral resolution is also gained through this illumination wavelength shift, as it is proportional to the ratio between the source's central wavelength λ_c and the objective's numerical aperture (NA). However, increasing the lateral resolution in conventional OCT systems reduces the depth-of-field (DOF) by restricting the confocal gating and effectively hampering the multiplexing advantage of Fourier domain OCT. As such, optical coherence microscopy¹⁸ (OCM), the high-NA version of OCT, might require an additional scan in depth to obtain 3-D images.^{19,20} This effect can be mitigated by splitting the illumination and detection modes of the OCM system and by illuminating the

sample with so-called diffractionless beams, such as Bessel beams.²¹ The resulting system, termed extended-focus OCM (xfOCM),²² performs 3-D images with a high lateral resolution maintained over larger DOFs than conventional OCM setups (typically 3 to 10× larger). Recently, we developed a high-resolution xfOCM platform, combining an ultrabroadband source spanning from the visible to the near-infrared wavelength range (from 500 to 850 nm) with high NA optics, to perform submicron resolution imaging of fixed brain slices and living cells.¹⁶ Although its high resolution enables resolving subcellular structures, its ~ 60 μm DOF limits its compatibility with *in vivo* cortical imaging. We therefore present a system based on our previous work, optimized for cortical imaging, where the lateral resolution was reduced to image over the entire penetration depth available with visible light (~ 150 μm). The system's resolution was characterized using a mirror and nanoparticles embedded in PDMS, and its imaging performance was assessed by imaging fine cerebral structures, such as myelinated axons, capillaries, and neuronal cells in the superficial somatosensory cortex of mice.

2 Methods

2.1 Extended-Focus Visible/Near-Infrared Optical Coherence Microscopy System

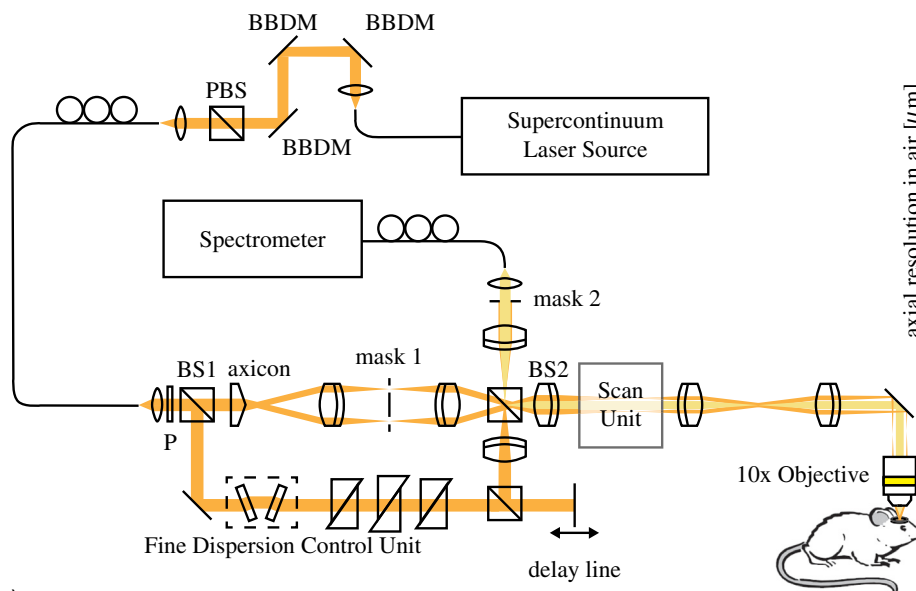
The extended-focus visible/near-infrared optical coherence microscopy (xf-visOCM) system presented here is based on previous xfOCM implementations^{16,22,23} and is optimized for high-resolution *in vivo* cortical imaging. Briefly, light from a supercontinuum source (Koheras SuperK Extreme, NKT Photonics) is first filtered to obtain an illumination spectrum from the visible to the near-infrared wavelength range, passes through a polarizing beam splitter (PBS) and is then coupled into the microscope. As shown in Fig. 1, at the microscope's

*Address all correspondence to: Paul J. Marchand, E-mail: paul.marchand@epfl.ch

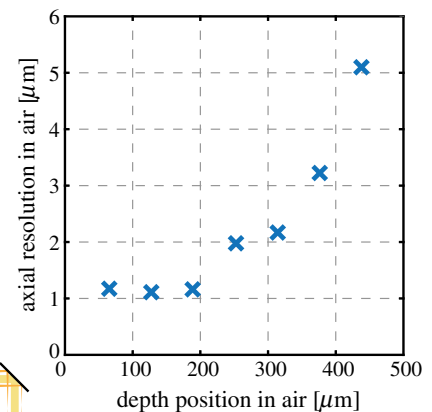
core lies a Mach-Zehnder interferometer to permit splitting the Bessel illumination and Gaussian detection modes. The first beam splitter (BS1) of the interferometric configuration divides the incoming light into the reference and the illumination arm, where an axicon (176 deg, Asphericon) transforms the initial Gaussian beam into a Bessel beam. A series of telescopes guides the illumination beam through a pair of galvanometric scanners and through the sample arm where it is finally focused on the sample (i.e., mouse cortex) through a 10× objective (NA = 0.3, UPlanFI, Olympus). The backscattered light from the sample is collected by the objective, descanned, and then guided to the Gaussian detection path by means of the second beam splitter of the Mach-Zehnder configuration (BS2), and finally coupled into the detection fiber and sent to the spectrometer. The reference arm comprises a set of prisms of different glasses (BK7,

SF6, and UVFS) to balance the dispersion present in the illumination and sample arms and the residual dispersion is precisely balanced through a fine-compensation unit.¹⁶ The interference between the reference and sample light is recorded by a custom spectrometer, comprising a grating (600 lines/mm, Wasatch Photonics), a custom objective (EFL = 100 mm), and a CMOS line camera (Basler, spL2048-140km). All 2048 pixels of the camera were used to record the spectral interferograms, spanning from 500 to 850 nm in wavelength. As shown in Fig. 1(a), a pair of masks are placed after the axicon lens and before the detection coupler to filter the spurious beams generated by the tip of the axicon and specular reflections originating from the sample, respectively. Moreover, the polarization state of the illumination was fixed using a PBS and a linear polarizer (P) placed at the entrance of the microscope. In

(a) xf-visOCM setup



(b) axial resolution in air



(c) lateral PSF in water

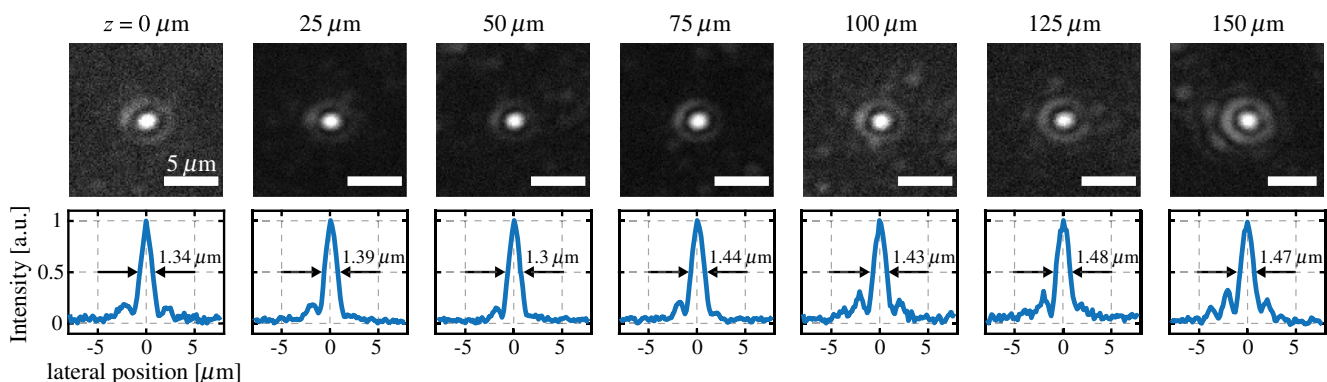


Fig. 1 xf-visOCM system and characterization: (a) schematic of the microscope based on a Mach-Zehnder interferometer comprised of two beam-splitters (BS1 and BS2) to split the Bessel illumination and the Gaussian detection paths. A fine-dispersion compensation unit in the reference arm enables precisely compensating the dispersion of the interferometer and a 10× air objective focuses the light in the cerebral cortex of a mouse. BBDM, broadband dielectric mirrors; PBS, polarized beam splitter; P, linear polarizer; BS, beam splitter. (b) The ultrabroadband visible/near-infrared spectrum of the xf-visOCM system provides an axial resolution in air of $\sim 1.1 \mu\text{m}$ over $\sim 200 \mu\text{m}$ in depth before deteriorating to $\sim 5 \mu\text{m}$ in air. (c) The FWHM of the lateral PSF of the xf-visOCM system is $\sim 1.4 \mu\text{m}$ in water and is maintained over $150 \mu\text{m}$ in depth through the extended-focus configuration, as shown by both the heatmaps and their corresponding profiles (in linear scales). Scalebar: $5 \mu\text{m}$.

practice, we observed that without this configuration, the visibility of the fringes of the interferogram was low and not constant throughout the spectrum. These effects can be attributed to the spectral and polarization-dependent transmission of certain optical elements, such as non polarising beamsplitters. By controlling the polarization of the illumination, the fringe visibility could ultimately be maximized.

2.2 Mouse Preparation

All the experiments were carried out in accordance to the Swiss legislation on animal experimentation (LPA and OPAN). The protocols (VD 3048) were approved by the cantonal veterinary authority of the canton de Vaud, Switzerland (SCAV, Département de la sécurité et de l'environnement, Service de

la consommation et des affaires vétérinaires) based on the recommendations issued by the regional ethical committee (i.e., the state committee for animal experiments of canton de Vaud) and are in-line with the 3Rs and follow the ARRIVE guidelines. The capabilities of the xf-visOCM system were assessed by imaging the superficial cortex of mice *in vivo*. To this intent, the cortex of $n = 3$ c57bl/6 mice (3 to 4 months old, Charles River) was made optically accessible through an open-skull craniotomy. Mice were first anesthetized using a solution of ketamine (80 to 100 mg/kg) and xylazine (14 mg/kg) injected intraperitoneally. Once asleep, their skull was exposed through an incision in the skin of their heads. A circular region of skull of 4 mm in diameter above the somatosensory cortex was drilled, excised, and then sealed using a glass coverslip and dental cement. Finally, a fixation ring was placed on the sealed cranial window to minimize

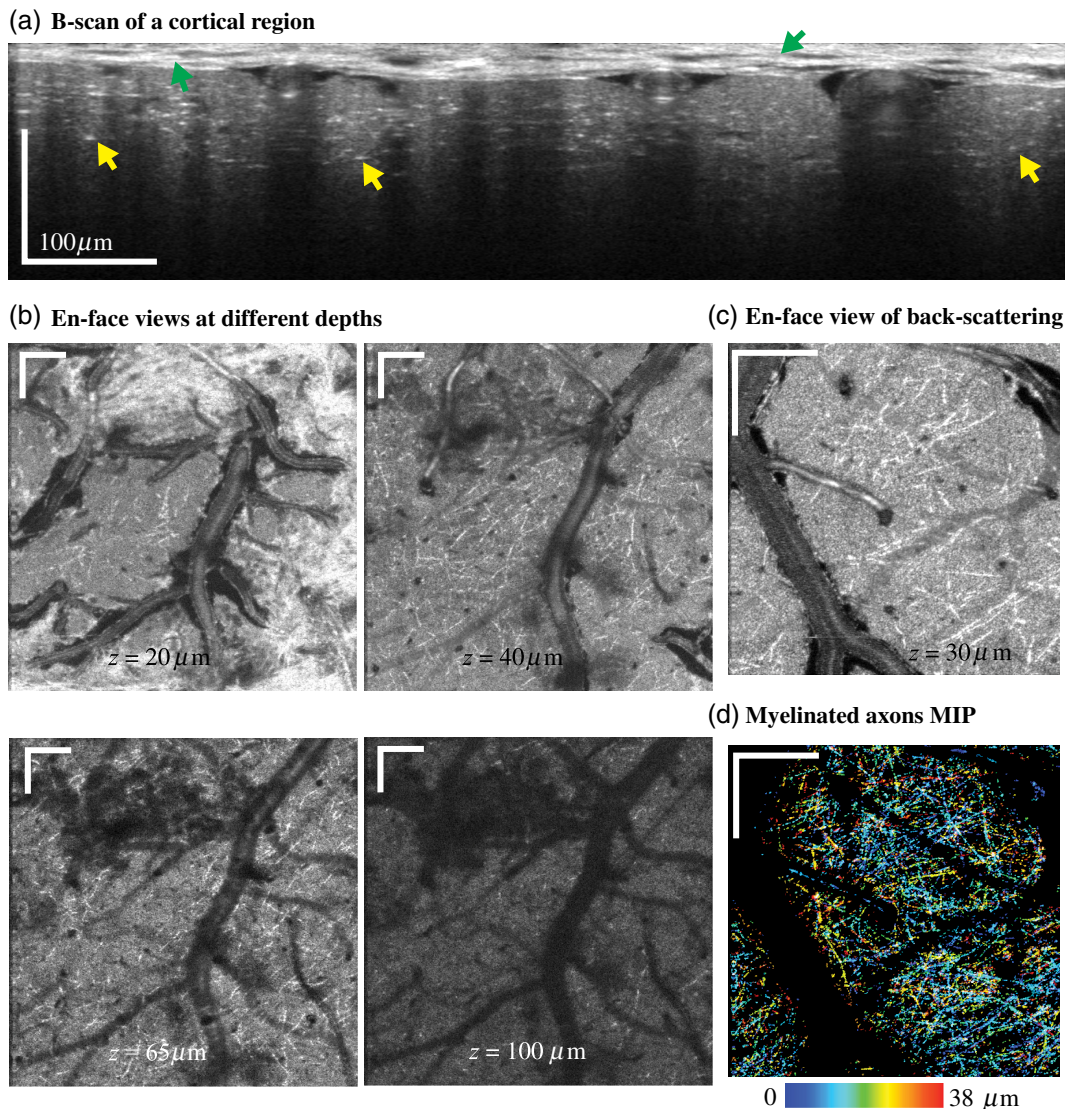


Fig. 2 xf-visOCM *in vivo* imaging: the imaging capabilities of the xf-visOCM system were assessed by imaging the superficial cortex of mice. (a) A B-scan across the first $\sim 100 \mu\text{m}$ in depth of the cortex highlights the different structures observable, such as bright, myelinated axons (pointed by yellow arrows), and dura mater (pointed by green arrows). (b) The *en face* views at different depths present the same structures as in (a) and show the preservation of the lateral resolution in depth. (c) In another animal, myelinated axons can also be visualized in the *en face* view at a depth of $30 \mu\text{m}$ from the cortical surface. (d) A depth-encoded view of segmented myelinated axons exposes the dense distribution of these fibers within the first layer of the brain. Scalebars: $100 \mu\text{m}$.

motion artifacts and facilitate the localization of the same cortical region over time. After the surgery, mice were allowed to recover for a period of a week. Prior to imaging, mice were anesthetized using the same ketamine/xylazine mixture as mentioned above and once asleep, were placed on a custom head fixation system for imaging. The mice's eyes were kept moist using eye ointment, and their body temperature was maintained at 36°C throughout the surgical procedure and the imaging sessions. Postoperative care consisted in daily subcutaneous injections of dexamethasone (0.2 mg/kg), carprofen (5 mg/kg), and buprenorphine (0.1 mg/kg) for 72 h from the day of the surgery.

3 Results

3.1 *xf-visOCM* Resolution Characterization

The system's axial resolution was assessed using a mirror placed on the sample holder and by changing the length of the reference arm. As shown in Fig. 1(b), an axial resolution of $\sim 1.1 \mu\text{m}$ in air ($\sim 0.85 \mu\text{m}$ in water) is preserved over the first $\sim 200 \mu\text{m}$ in air ($\sim 150 \mu\text{m}$ in water) before significantly increasing and reaching $> 5 \mu\text{m}$ by $\sim 400 \mu\text{m}$ in air. The axial resolution was measured as the full-width at half-maximum (FWHM) of the axial point spread function (PSF) in linear scale. The lateral PSF of the

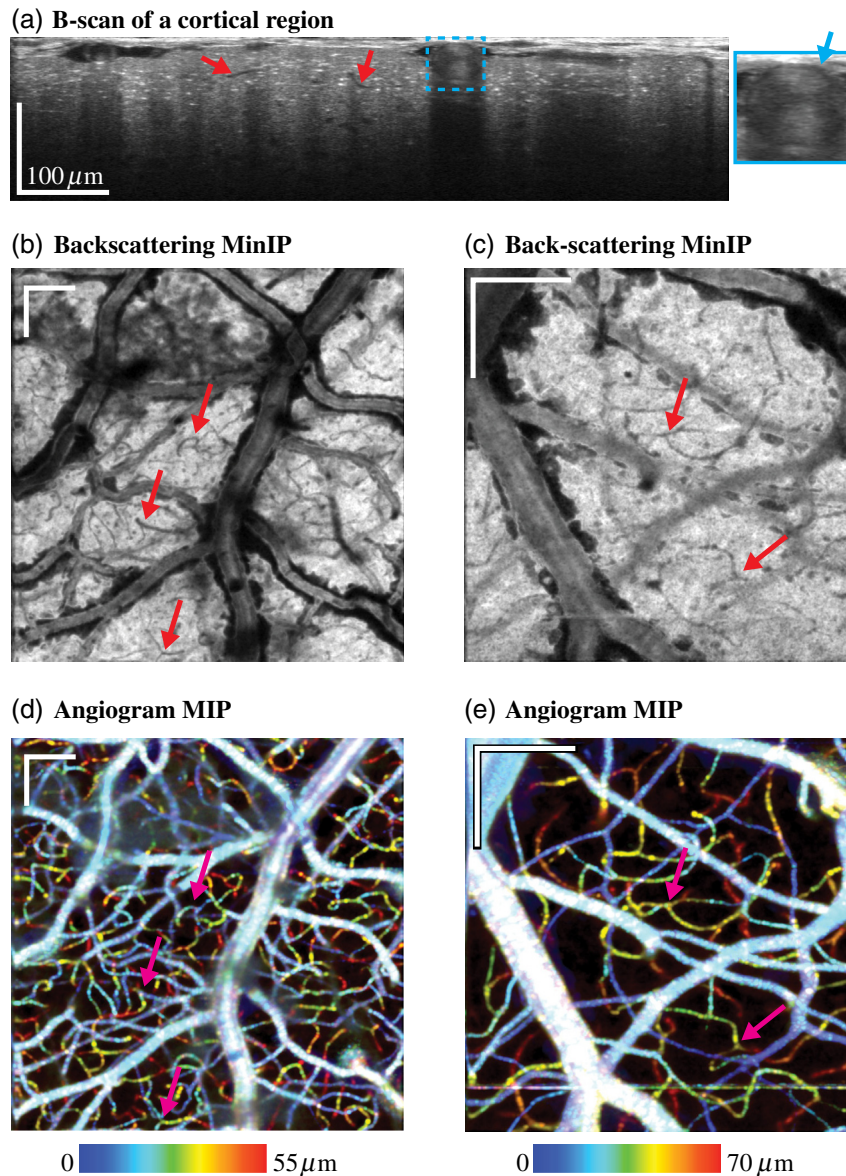


Fig. 3 *xf-visOCM* *in vivo* vascular imaging: owing to the high resolution of the *xf-visOCM* system, the microvasculature can be resolved both in the backscattering tomograms and in the angiograms. (a) A B-scan covering the first $\sim 100 \mu\text{m}$ in depth of the cortex reveals large vessels at the surface and capillaries that can be resolved as dark elongated structures, as pointed by the red arrows. Moreover, a close-up on the large caliber vessel reveals a thin dark cell-free layer below the vessels membrane (blue arrow). Vascular structures can be visualized by either performing a minimum intensity projection on the static backscattering, in (b) and (c), or an MIP on the angiogram, (d) and (e). Similar features are highlighted between the two visualizations by red arrows in (b) and (c) and pink arrows in (d) and (e). Scalebars: $100 \mu\text{m}$.

system was interrogated by imaging a sample of 30 nm gold nanoparticles embedded in PDMS. From the acquired data, an average PSF for seven different depths was obtained by extracting and averaging over five individual PSFs at each plane. The resulting PSFs over depth are displayed in Fig. 1(c), where the FWHM of the central lobe is maintained at $\sim 1.4 \mu\text{m}$ over $150 \mu\text{m}$ in depth. At larger depths, the PSF slightly broadens due to the presence of additional sidelobes and by a decrease in the signal intensity (observable here through an increase in the background noise). This loss in intensity is caused by a combination of the shape of the axial profile of the Bessel beam and by the Gaussian apodization²⁴ and by the system's roll-off.

3.2 *In Vivo* Imaging of Cortical Structures

With the system characterized, the imaging performance of the xf-visOCM platform was assessed by imaging the superficial cortex of mice. All images presented in this paper were acquired at a line rate of 20 kHz, with an incident power on the sample of 0.5 mW and were averaged over five volumetric acquisitions, i.e., C-scans. The imaging time for a single volumetric acquisition was from 2 to 4 min. Figures 2(a) and 2(b) show a B-scan and *en face* views at different depths of the superficial cortex, respectively. Similarly to previous observations of cortical structures using OCT,^{3,6,15–17,20,25,26} dura mater (highlighted by green arrows) and myelinated axons (pointed by yellow arrows) are characterized by a stronger backscattering than the neuropil and appear as bright layers and fibers, respectively. The extended-focus capabilities of the system are illustrated in the *en face* views presented in tile (b) showing the ability to resolve the fine bright myelinated axons throughout a depth of $80 \mu\text{m}$.

Myelinated axons can also be visualized at a depth of $30 \mu\text{m}$ from the cortical surface in another animal, as shown in Fig. 2(c). In addition, through their increased backscattering, these structures could be segmented from the parenchyma using a simple thresholding operation, similarly to Merkle et al.¹⁵ By adapting the threshold for attenuation in depth, the axons were segmented at different depths to obtain a depth-encoded maximum intensity projection (MIP) as shown in Fig. 2(d).

In addition to imaging neural fibers, the high resolution of the system permits discriminating fine features such as capillaries and the boundary of large vessels from the surrounding background. A fine dark region can be discerned within large vessels, below their membranes [blue arrow in Fig. 3(a)], as previously reported by Merkle et al.¹⁵ and identified as a cell-free layer within the lumen of large caliber vessels. Similarly to our previous work in *ex-vivo* slices at higher lateral resolution,¹⁶ the lumen of capillaries can be distinguished from the neuropil as dark elongated structures, as shown by the red arrows in Fig. 3(a) and by the red arrows in the minimum intensity projections (MinIP) shown in Figs. 3(b) and 3(c) and 4(c). In contrast to slices where the reduced intensity was linked to the absence of scatterers in the lumen of the vessels, here the reduced backscattering seems to be caused by the dynamic nature of the scattering of red blood cells (RBC). The images displayed Figs. 3 and 4 were obtained by averaging 8 to 16 B-scans acquired at the same lateral position (in addition to the $5\times$ averaging over C-scans) and represent the low-pass filtered component of the backscattering (i.e., its static component). Therefore, due to the motion and discrete nature of RBCs flowing in capillaries,²⁷ the static contribution of their

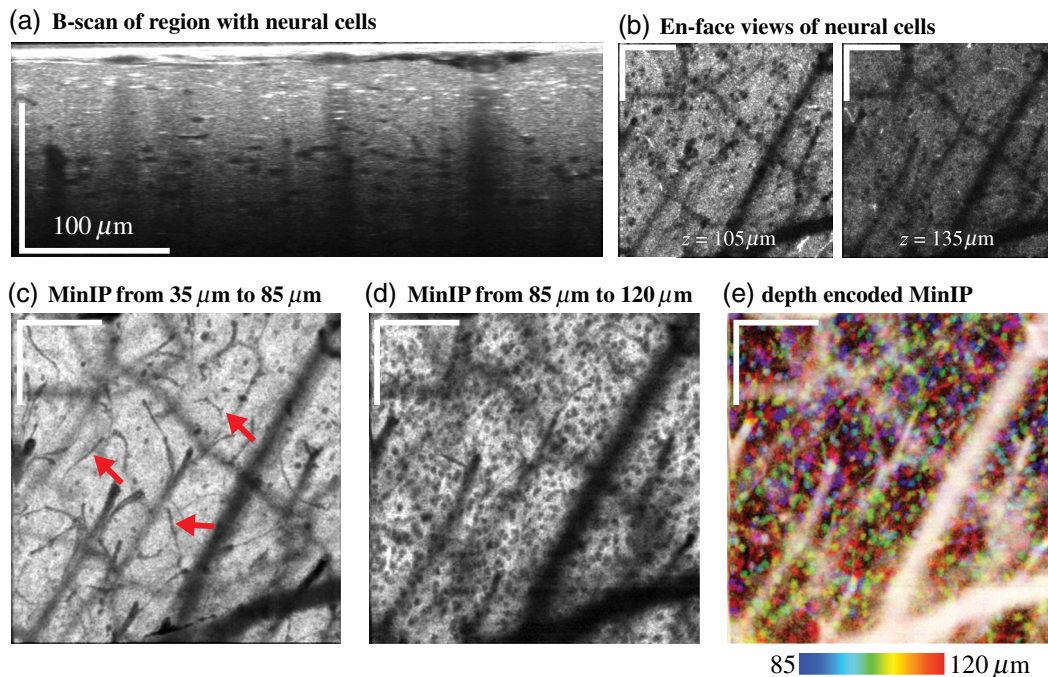


Fig. 4 xf-visOCM *in vivo* imaging of neural cells: neural cells can be identified in (a) the backscattering B-scan and (b) *en face* views as dark spheroids surrounded by the neuropil. These cells can be identified up to a depth of $\sim 135 \mu\text{m}$. (c) Fine features can be further visualized through minimal intensity projections, highlighting the presence of mainly vascular structures from 35 to $85 \mu\text{m}$ in depth, and (d) neural cells from $85 \mu\text{m}$ and beyond. (c) Capillaries can be identified in the MinIP by their hollow lumen, as highlighted by the red arrows in tile. (e) The spatial distribution of these cell bodies can be appreciated by a depth color coded minimum intensity projection. Scalebars: $100 \mu\text{m}$.

backscattering is weaker than that of the surrounding parenchyma and appears darker than the tissue. The final pixel size of every *en face* image shown in Figs. 2–4 after filtering is 512×512 .

Conversely, an angiogram, as shown in Figs. 3(d) and 3(e), can be obtained by filtering out the static component of the backscattering^{28,29} (over 8 and 16 B-scan repetitions, respectively). The high-pass filtering operation was performed through a pointwise complex subtraction of each B-scan.²⁸ The depth-encoded MIPs shown in Figs. 3(d) and 3(e) were obtained by normalizing the angiogram with the structure as described by Srinivasan et al.^{2,19} to account for the reduced intensity in depth and alleviate the impact of bright structures in the shadows of large vessels [here mainly bright myelinated axons in the shadows of vessels, visible as bright dots in Fig. 3(e)]. These angiograms highlight the presence of large pial vessels at the surface and the beginning of the cortical microvascular meshwork in deeper regions. Moreover, the location of capillaries in the angiogram coincides with the dark elongated structures reported in the MinIP Figs. 3(b) and 3(c) of the same figure (highlighted by the red and pink arrows on Figs. 3(d) and 3(e), respectively), reinforcing our observation that capillaries can be distinguished as darker structures in the backscattering images.

In contrast to OCT systems operating at longer wavelengths, the penetration depth of visible light is reduced to $\sim 150 \mu\text{m}$ in tissue.^{9,30} Nevertheless, as shown in Fig. 4, cell bodies located at $\sim 100 \mu\text{m}$ in depth can be resolved in the B-scan and in the *en face* views presented in tiles (a) and (b) (temporally averaged frames). Similarly to other observations of cell bodies in the visible range and using other illumination spectra,^{4,17,19,20,26} these cell bodies appear as spheroids with a lower intensity than the surrounding parenchyma, and their visualization can be further enhanced through a minimum intensity projection, as shown in Figs. 4(d) and 4(e). Moreover, MinIPs at different depths, as shown in Figs. 4(c)–4(e), hint to the laminar organization of the cortex, where the first $\sim 85 \mu\text{m}$ are almost devoid of these cell bodies and display a sparse microvascular network, whereas deeper regions show a dense population of cells. Figures 4(d) and 4(e) were obtained by shifting the focus slightly deeper within the cortex, to counteract the attenuation of light. Overall, the shape, contrast, and depth distribution [highlighted in Fig. 4(e)] of these cells coincide with the presence of neural cells in the first part of layer II/III of the rodent cortex.^{4,19,26}

4 Conclusion and Discussion

In this paper, we presented an extended-focus OCM system operating from the visible to the near-infrared wavelength range and optimized for *in vivo* superficial cortical imaging. Although its illumination spectrum inherently limits the depth penetration abilities of the platform, the coherent amplification property of OCT enables imaging up $\sim 150 \mu\text{m}$. As shown in the system's characterization, the extended-focus configuration maintains a lateral PSF FWHM of $\sim 1.4 \mu\text{m}$ over the entire available penetration depth, and the ultrabroadband spectrum offers a submicron $\sim 0.85 \mu\text{m}$ axial resolution. Although dispersion was balanced between both arms of the interferometer, additional dispersion caused by tissue could affect the optical sectioning at large depths. Moreover, as shown in Fig. 1(b), the axial resolution degrades rapidly beyond $>200 \mu\text{m}$ from the zero delay line and could further deteriorate the system's performance. Future improvements on the setup will involve using longer

line cameras (i.e., with more pixels) to improve the spectrum's sampling as used by Lichtenegger et al.⁹ We used the system to image the first layers of the somatosensory cortex of mice, showing the ability of the xf-visOCM system to resolve cerebral structures such as myelinated axons, vessels through both static and dynamic backscattering, and neural cells. The combined extended-focus property of the Bessel–Gauss configuration and the broadband spectrum enabled imaging at a high lateral resolution over the entire penetration depth and at a submicron axial resolution. Overall, we believe that the performance and imaging capabilities of the xf-visOCM system make it an attractive tool to study cerebral physiology in health and in disease,^{3,31} *in vivo*, and at high resolution.

Disclosures

The authors declare that there are no conflicts of interest and no competing interests related to this article.

Acknowledgments

This study was partially supported by the Commission for Technology and Innovation (13964.1 PFLS-LS and 17537.2 PFLS-LS), the Swiss National Science Foundation (205321L_135353 and 205320L_150191) and the EU Framework Programme for Research and Innovation (686271/SEFRI 16.0047).

References

1. A. F. Fercher et al., "Optical coherence tomography—principles and applications," *Rep. Prog. Phys.* **66**, 239–303 (2003).
2. V. J. Srinivasan et al., "Optical coherence tomography for the quantitative study of cerebrovascular physiology," *J. Cereb. Blood Flow Metab.* **31**, 1339–1345 (2011).
3. T. Bolmont et al., "Label-free imaging of cerebral β -amyloidosis with extended-focus optical coherence microscopy," *J. Neurosci.* **32**, 14548–14556 (2012).
4. J. Lee et al., "Quantitative imaging of cerebral blood flow velocity and intracellular motility using dynamic light scattering-optical coherence tomography," *J. Cereb. Blood Flow Metab.* **33**, 819–825 (2013).
5. U. Baran, Y. Li, and R. K. Wang, "Vasodynamics of pial and penetrating arterioles in relation to arteriolo-arteriolar anastomosis after focal stroke," *Neurophotonics* **2**(2), 025006 (2015).
6. C. Magnain et al., "Optical coherence tomography visualizes neurons in human entorhinal cortex," *Neurophotonics* **2**(1), 015004 (2015).
7. F. E. Robles et al., "Molecular imaging true-colour spectroscopic optical coherence tomography," *Nat. Photonics* **5**(12), 744–747 (2011).
8. X. Shu, L. Beckmann, and H. F. Zhang, "Visible-light optical coherence tomography: a review," *J. Biomed. Opt.* **22**(12), 121707 (2017).
9. A. Lichtenegger et al., "Spectroscopic imaging with spectral domain visible light optical coherence microscopy in Alzheimer's disease brain samples," *Biomed. Opt. Express* **8**(9), 4007–4025 (2017).
10. J. Yi et al., "Visible-light optical coherence tomography for retinal oximetry," *Opt. Lett.* **38**(11), 1796–1798 (2013).
11. S. P. Chong et al., "Structural and functional human retinal imaging with a fiber-based visible light OCT ophthalmoscope," *Biomed. Opt. Express* **8**(1), 323–337 (2017).
12. S. P. Chong et al., "Quantitative microvascular hemoglobin mapping using visible light spectroscopic optical coherence tomography," *Biomed. Opt. Express* **6**(4), 1429–1450 (2015).
13. S. Chen et al., "Imaging hemodynamic response after ischemic stroke in mouse cortex using visible-light optical coherence tomography," *Biomed. Opt. Express* **7**(9), 3377–3389 (2016).
14. J. Yi et al., "Human retinal imaging using visible-light optical coherence tomography guided by scanning laser ophthalmoscopy," *Biomed. Opt. Express* **6**(10), 3701–3713 (2015).
15. C. W. Merkle et al., "Visible light optical coherence microscopy of the brain with isotropic femtoliter resolution *in vivo*," *Opt. Lett.* **43**(2), 198–201 (2018).

16. P. J. Marchand et al., "Visible spectrum extended-focus optical coherence microscopy for label-free sub-cellular tomography," *Biomed. Opt. Express* **8**(7), 3343–3359 (2017).
17. O. Assayag et al., "Imaging of non-tumorous and tumorous human brain tissues with full-field optical coherence tomography," *Neuroimage Clin.* **2**(1), 549–557 (2013).
18. J. A. Izatt et al., "Optical coherence microscopy in scattering media," *Opt. Lett.* **19**(8), 590–592 (1994).
19. V. J. Srinivasan et al., "Optical coherence microscopy for deep tissue imaging of the cerebral cortex with intrinsic contrast," *Opt. Express* **20**, 2220–2239 (2012).
20. C. Leahy, H. Radhakrishnan, and V. J. Srinivasan, "Volumetric imaging and quantification of cytoarchitecture and myeloarchitecture with intrinsic scattering contrast," *Biomed. Opt. Express* **4**, 1978–1990 (2013).
21. Z. Ding et al., "High-resolution optical coherence tomography over a large depth range with an axicon lens," *Opt. Lett.* **27**(4), 243–245 (2002).
22. R. A. Leitgeb et al., "Extended focus depth for Fourier domain optical coherence microscopy," *Opt. Lett.* **31**(16), 2450–2452 (2006).
23. M. Villiger, C. Pache, and T. Lasser, "Dark-field optical coherence microscopy," *Opt. Lett.* **35**(20), 3489–3491 (2010).
24. M. Villiger and T. Lasser, "Image formation and tomogram reconstruction in optical coherence microscopy," *J. Opt. Soc. Am.* **27**(10), 2216–2228 (2010).
25. J. B. Arous et al., "Single myelin fiber imaging in living rodents without labeling by deep optical coherence microscopy," *J. Biomed. Opt.* **16**(11), 116012 (2011).
26. S. Tamborski et al., "Extended-focus optical coherence microscopy for high-resolution imaging of the murine brain," *Biomed. Opt. Express* **7**(11), 4400–4414 (2016).
27. J. Lee et al., "Multiple-capillary measurement of RBC speed, flux, and density with optical coherence tomography," *J. Cereb. Blood Flow Metab.* **33**, 1707–1710 (2013).
28. V. J. Srinivasan et al., "Rapid volumetric angiography of cortical microvasculature with optical coherence tomography," *Opt. Lett.* **35**, 43–45 (2010).
29. C.-L. Chen and R. K. Wang, "Optical coherence tomography based angiography [Invited]," *Biomed. Opt. Express* **8**(2), 1056–1082 (2017).
30. S. P. Chong et al., "Noninvasive, in vivo imaging of subcortical mouse brain regions 1.7 μm with optical coherence tomography," *Opt. Lett.* **40**(21), 4911–4914 (2015).
31. A. J. Schain, R. A. Hill, and J. Grutzendler, "Label-free in vivo imaging of myelinated axons in health and disease with spectral confocal reflectance microscopy," *Nat. Med.* **20**, 443–449 (2014).

Paul J. Marchand is a graduate student at the Laboratoire d'Optique Biomédicale of Prof. Theo Lasser at EPFL Lausanne. He received his BSc degree in microengineering from EPFL in 2010, his MSc degree in nanotechnologies in 2012 from Politecnico di Torino, INPG Grenoble and EPFL and his MSc degree in biomedical engineering in 2013 from Imperial College London. His current research interests include coherent imaging and optical microscopy to study cerebral physiology.

Daniel Szlag received his MSc degree in technical physics and completed the three-year studies of applied informatics at Nicolaus Copernicus University, Poland. In 2014, he received his PhD in biophysics as a result of Sciex scholarship and research conducted at EPFL Lausanne in Biomedical Optics Laboratory of Professor Theo Lasser. His research is focused on optical imaging systems design and methods for life science and industrial applications.

Arno Bouwens obtained his PhD at the École Polytechnique Fédérale de Lausanne (EPFL). Currently, he is a postdoctoral researcher at EPFL and KU Leuven. His research interests include optical coherence tomography, phase microscopy, and applications of super-resolution microscopy.

Theo Lasser is a full professor and head of the Laboratoire d'Optique Biomédicale in the Department of Microengineering of EPFL. He also has many years of experience in industry and more particularly in Carl Zeiss, where he served as head of R&D and general manager. His research is mainly focused on the development of optical functional imaging methods for applications in life sciences and medicine.